

Chemo-physical properties of asbestos bodies in human lung tissues studied at the nano-scale by non-invasive, label free x-ray imaging and spectroscopic techniques



Fabrizio Bardelli^{a,*}, Francesco Brun^b, Simone De Panfilis^c, Peter Cloetens^d,
Silvana Capella^{e,f}, Elena Belluso^{e,f}, Donata Bellis^{f,g}, Arianna Di Napoli^h, Alessia Cedola^a

^a Institute of Nanotechnology – CNR-Nanotec, c/o Department of Physics, Sapienza University, Roma, Italy

^b Department of Engineering and Architecture, University of Trieste, Trieste, Italy

^c Center for Life Nano- & Neuro-Science, Fondazione Istituto Italiano di Tecnologia (IIT), Roma, Italy

^d European Synchrotron Radiation Facility (ESRF), Grenoble, France

^e Department of Earth Sciences, University of Torino, Torino, Italy

^f Interdepartmental Centre for the Study of Asbestos and Other Toxic Particulate “G. Scansetti”, University of Torino, Torino, Italy

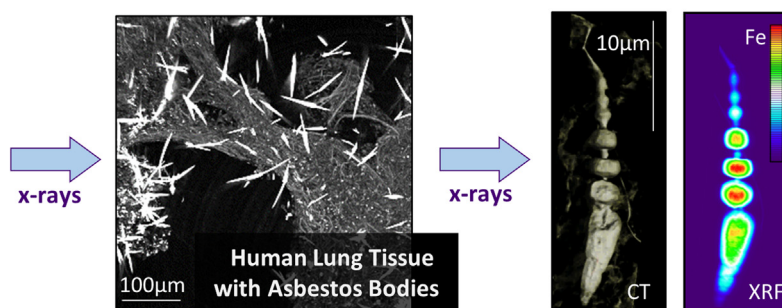
^g Department of Surgery, Pathological Anatomy, Ospedale degli Infermi, Biella, Italy

^h Department of Clinical and Molecular Medicine, Pathology Unit, Sant’Andrea Hospital, Sapienza University, Rome, Italy

HIGHLIGHTS

- Unaltered lung tissue samples from former asbestos workers were studied.
- Combined x-ray tomography and x-ray spectroscopy were exploited.
- The 3D morphology and mass density of selected asbestos bodies were revealed.
- Quantitative elemental analysis revealed similar composition of the asbestos bodies.
- The Fe content in the asbestos bodies was higher than that contained in asbestos.

GRAPHICAL ABSTRACT



ARTICLE INFO

Article history:

Received 4 February 2021

Received in revised form 17 May 2021

Accepted 18 May 2021

Editor: Dr. Angela Mally

Available online 20 May 2021

Keywords:

Asbestos

Lungs

Imaging

Tomography

ABSTRACT

In the lungs, asbestos develops an Fe-rich coating (Asbestos Body, AB) that becomes the actual interface between the foreign fibers and the host organism. Conventional approaches to study ABs require an invasive sample preparation that can alter them. In this work, a novel combination of x-ray tomography and spectroscopy allowed studying unaltered lung tissue samples with chrysotile and crocidolite asbestos. The thickness and mass density maps of the ABs obtained by x-ray tomography were used to derive a truly quantitative elemental analysis from scanning x-ray fluorescence spectroscopy data. The average mass density of the ABs is compatible with that of highly loaded ferritin, or hemosiderin. The composition of all ABs analyzed was similar, with only minor differences in the relative elemental fractions. Silicon concentration decreased in the core-to-rim direction, indicating a possible partial dissolution of the inner fiber. The Fe content in the ABs was higher than that possibly contained in chrysotile and crocidolite. This finding opens two opposite scenarios, the first with Fe coming from the

* Corresponding author.

E-mail address: fabrizio.bardelli@uniroma1.it (F. Bardelli).

1. Introduction

Prolonged exposure to asbestos is known to induce malignant mesothelioma (MM), an aggressive neoplasia of the lung serosal lining, asbestosis, and other severe lung diseases (Jones et al., 1996; Klebe et al., 2020; Noonan, 2017; Uguen et al., 2017). The numbers of the asbestos-related diseases are impressive: in the United States, MM is responsible for approximately ~3000 deaths per year (Mazurek et al., 2017), and the figure rises to almost 7000 in Western Europe (Kameda et al., 2014). The US National Institute of Health estimated that over 20 million people are at risk of developing MM due to asbestos exposure in US only (Carbone et al., 2012). It is important to highlight that the asbestos threat is still a current major health risk worldwide (Carbone et al., 2012). The main reason of this is the long latency from the beginning of the exposure to asbestos to the development of MM (20–40 years, on average (Reid et al., 2014)). Moreover, the weathering of existing asbestos products (Capella et al., 2020; Spurny, 1989) and naturally occurring asbestos (NOA) (Bloise et al., 2016b; Fantauzzi et al., 2012) continue to contribute to the asbestos hazard. As a consequence, mortality rates continued to increase by 5–10% per year in most industrialized countries (Abdel-Rahman, 2018; Bianchi and Bianchi, 2014; Carbone et al., 2019, 2012; Park et al., 2011), despite most countries started to ban asbestos production and commercialization between the 1970s and the 1990s.

Asbestos is a commercial term referring to a group of naturally occurring fibrous minerals, namely five amphiboles [amosite (grunerite), crocidolite (riebeckite), anthophyllite, tremolite, and actinolite] and one serpentine (chrysotile). Thanks to their small dimensions (10–100 μm in length, and 0.2–0.4 μm in diameter (Hwang and Gibbs, 1981)) amphibole and chrysotile asbestos can reach the innermost lungs structures by inhalation, where amphibole asbestos can remain for life-long thanks to its high bio-persistence (Di Giuseppe et al., 2019; Giacobbe et al., 2021; Pacella et al., 2014).

In the lungs, alveolar macrophages have the role of removing foreign particles, and are able to do it efficiently when dealing with common micron-sized particulate matter (Gawda et al., 2018). However, due to their limited size (10–15 μm in humans) the macrophages are not able to completely engulf high aspect ratio materials with length $>\sim 10 \mu\text{m}$ and width $<\sim 0.5 \mu\text{m}$, and so to remove them from the host organism (Boulanger et al., 2014). The resulting frustrated phagocytosis initiates an *in vivo* biomineralization process leading to the deposition of organic and inorganic material, and to the formation of peculiar structures consisting of an Fe-rich envelope surrounding the original fibers. These structures are commonly referred to as Asbestos Bodies (ABs in the following) (Churg and Warnock, 1981; Davis, 1964; Gloyne, 1931a; Pooley, 1972).

Despite the link between exposure to asbestos and MM has already been demonstrated between the 1950s and the 1970s (Wagner et al., 1974, 1960), little advancements were made in medical treatments, and still nowadays only one person over twenty is alive five years after MM diagnosis, (i.e. 5-year survival rate of 5%). Asbestos Bodies were initially believed to be the effort of the host organism to isolate the foreign fibers (Ghio et al., 1997; Mace et al., 1980; McLemore et al., 1980). However, other works suggested that they might enhance the cytotoxic properties of asbestos, showing that no consensus has been yet reached on their pathogenetic role. In particular, *in vitro* and *in vivo* experiments

(respectively, with cell cultures and animals), showed that ABs are able to induce the generation of free radicals (Ghio et al., 2008; Governa and Amati, 1999; Pacella et al., 2012), double strand breaks in the DNA (Lund et al., 1994), and that the iron contained in the coating is catalytically active (Fubini and Mollo, 1995; Governa and Amati, 1999; Hardy and Aust, 1995). Even if key mechanisms by which asbestos would start the chain of events leading to MM have been proposed (Andreozzi et al., 2017; Pacella et al., 2015, 2010; Yang et al., 2010, 2006), less attention was devoted to the role of the ABs. Indeed, it is reasonable to believe that the ABs may play role in the pathogenesis, as they start to form soon after (weeks/months) asbestos reaches the lungs (Barrett et al., 1989), thus quickly becoming the actual interface between asbestos and the biological tissues. Moreover, the long latency time of MM (decades), opposed to its rapid evolution and fatal outcome once it sets in (months), implies that there is a long period of time during which it may be possible to arrest or delay the carcinogenic process (Carbone et al., 2019; Toyokuni, 2014).

Due to their dimensions, nanoprobe techniques with high sensitivity (few ppm) and sub-micron spatial resolution are required to study the ABs. Early works (Gloyne, 1929, 1931b), in the 1930s succeeded in imaging single ABs by electron microscopies, obtaining the basic information on their morphology and main components: a central fiber surrounded by an Fe-coating. Later works, in the 1960s (Davis, 1964; Pooley, 1972; Suzuki and Churg, 1969), brought in essential knowledge about the ABs composition and formation mechanism, suggesting that the coating is mainly composed of ferritin and/or hemosiderin deposited on asbestos by the alveolar macrophages or other cells in the attempt to digest or isolate the fibers. The success of early works was based on complex sample preparation protocols, meticulously executed. This approach, however, was also their main limitation, as either the ABs had to be recovered from the tissues with invasive methods such as chemical digestion, or the tissue had to be sectioned in ultra-thin slices ($\sim 50\text{--}100 \text{ nm}$), and embedded in suitable supports. Recently, there have been attempts to preserve the native state of the ABs under investigation and to reveal differences with those extracted by conventional chemical extraction procedures (Bardelli et al., 2017; Borelli et al., 2007). However, in the years, the question that remained unanswered is if, and to what extent, invasive sample preparation methods could alter the chemical and structural properties of the ABs.

In the last decade, a novel approach, requiring minimal samples manipulation, but with a spatial resolution comparable to that of electron microscopies (down to $\sim 10 \text{ nm}$), and a sensitivity down to that of bulk laboratory techniques (in the sub-ppm range), was exploited to study asbestos in biological samples based on x-ray micro and nanoprobe tools (Bardelli et al., 2017; Gianoncelli et al., 2013; Gualtieri et al., 2017; Pascolo et al., 2013, 2011; Pollastri et al., 2016a). The strength of the present work relies on the combination of two x-ray imaging and spectroscopic techniques, namely scanning X-ray Fluorescence spectroscopy (S-XRF) and X-ray Phase-Contrast holo-Tomography (XPChT), to study unaltered lung tissue samples from former asbestos workers. A unique advantage of the phase-contrast mode is the ability to image low absorbing materials, such as biological tissues, with higher contrast compared to conventional absorption imaging, as the magnitude of the variations in the phase shifts can be orders of magnitude higher than the absorption ones (Cloetens et al., 1999;

Khimchenko et al., 2018; Zabler et al., 2005). Scanning x-ray-induced fluorescence spectroscopy, on the other hand, is a label-free multi-elemental imaging technique able to reveal the elemental composition and distribution with high lateral resolution (~ 80 nm (Khimchenko et al., 2018)). Scanning X-ray fluorescence spectroscopy and XPChT were performed on the same tissue fragments containing ABs, allowing to obtain complementary information. In particular, the quantitative results of XPChT (thickness and mass density of the ABs) were used to perform a fully quantitative and reliable elemental analysis.

2. Materials and methods

Lung tissue samples were obtained *post-mortem* from the lower lobes of two former workers with a history of occupational exposure to asbestos (Table 1). Only non-neoplastic tissue samples were collected and preserved in buffered formalin (10 %). The workers were subjected to prolonged exposure (> 10 years) to an admixture of different asbestos phases, including amphibole (crocidolite, ideal chemical formula $\text{Na}_2(\text{Fe}^{2+}, \text{Mg})_3(\text{Fe}^{3+})_2\text{Si}_8\text{O}_{22}(\text{OH})_2$, and amosite, ideally $(\text{Fe}^{2+}, \text{Mg})_7\text{Si}_8\text{O}_{22}(\text{OH})_2$ (Fantauzzi et al., 2012)), and serpentine asbestos (chrysotile, ideally $\text{Mg}_3\text{Si}_2\text{O}_5(\text{OH})_4$ (Fantauzzi et al., 2012)). This was confirmed by Energy Dispersive Spectroscopy (EDS) measurements coupled with a Scanning Electron Microscope (SEM), which were performed on fibers extracted by chemical digestion and filtration of the tissue samples and determined that crocidolite was largely the prevalent fiber present (Fig. S1). A few EDS spectra were compatible with amosite, but its presence remains uncertain. No fibers with EDS spectra compatible with chrysotile were found. The workers developed severe-grade asbestos-related diseases (asbestosis, mesothelioma or lung cancer, pleural-plaques). The ABs per gram of dry weight (g_{dw}) of tissue (Table 1) was estimated following the method described in Belluso et al. (Belluso et al., 2006), which consists of digesting 1 g of formalin-fixed lung tissue with sodium hypochlorite (NaClO) and recovering the ABs by filtration through microporous membranes ($0.45 \mu\text{m}$ pore size).

In all samples, the burden of ABs largely exceeded the amount established by the European Respiratory Society guidelines to indicate a high level of occupational exposure to asbestos ($10^3/g_{\text{dw}}$) (De Vuyst et al., 1998). For XPChT measurements, $10 \mu\text{m}$ -thick sections were cut with a microtome from the paraffin blocks containing the formalin-fixed lung tissue. The sections were then de-paraffinized by heating at 60°C and washing with xylene, and then deposited on microscope slides covered with a $4 \mu\text{m}$ -thick polyethylene naphthalate (PEN) film. A laser micro-dissector (optical microscope coupled with a laser system) was used to cut fragments of $\sim 100 \mu\text{m}$ lateral size, containing at least one AB. These PEN-supported tissue fragments were glued edge-to-tip to $4 \mu\text{m}$ -tip borosilicate glass capillaries with 1.5 mm outer diameter (Fig. S2).

Combined XPChT and S-XRF acquisitions were performed at the ID16A Nano-Imaging beamline (Cesar da Silva et al., 2017; Gramaccioni et al., 2020) at the European Synchrotron Radiation Facility (ESRF). The beamline technical details can be found in the Supplementary Data. The measurements were performed in high vacuum at an incident x-ray energy of 17.05 keV . As required by the holo-tomography approach, each tomogram was acquired using in-line free space propagation mode at four different sample-to-detector distances, allowing obtaining quantitative information on the phase shift experienced by the x-rays crossing the sample, in addition to the conventional absorption contrast. For each tomogram, 1800 projections were acquired over a $0\text{--}180^\circ$ rotation range, with $0.07 \times 0.07 \times 0.07 \mu\text{m}^3$ isotropic voxel size and 0.1 s dwell time, resulting in a total exposure time per tomogram of 12 min . The field-of-view (FOV) was $143 \times 143 \times 126 \mu\text{m}^3$. For each sample, the four acquisitions were given as input to the multiple-distance phase-retrieval algorithms (Cloetens et al., 1999), available through ESRF in-house software using the GNU Octave programming environment (www.octave.org). Tomographic reconstruction of the phase maps was carried out using standard filtered back-projection, and data post-treatments and analyses were performed mainly using the ImageJ software package (Schneider et al., 2012). Holo-tomography is a measure of the electronic density, and, if the Guinier approximation ($Z/A \sim 0.5$, where Z is the atomic number and A the atomic weight) is fulfilled (Guinier and Physics, 1994), it is possible to convert the electronic density to the mass density. Scanning XRF measurements were conducted on the same beamline and on the same samples, using the same incident energy and sample-holder. Measurements were performed in raster scanning mode, using a 6-element x-ray fluorescence Si-drift detector placed at distance of 36 mm from the sample. The pixel size was 0.15×0.15 or $0.05 \times 0.05 \mu\text{m}^2$, and the integration time per pixel was set to 0.05 s . Several hours were necessary to complete an acquisition of a $\sim 100 \times 100 \mu\text{m}^2$ map in raster scan mode. The incident photon energy (17.05 keV) allowed exciting and detecting elements in the atomic number range Z between 13 and 39 (K fluorescence lines of elements from Al to Y), and between 40 and 84 (L fluorescence lines of elements from Zr to Po). The fluorescence efficiency of elements lighter than Al is too low to be reliably detected at the chosen incident energy, and the beryllium windows between the sample and the detector further reduce their signal. A dedicated beamline Python script was used to correct the XRF maps for detector dead time and perform normalization for the incident x-ray beam. The script then calls the PyMCA software package (Solé et al., 2007) to perform a pixel by pixel fit of the fluorescence spectra. The elements included in the fits were Si, P, S, Cl, K, Ca, Ti, Cr, Fe, Ni, Zn, Se, As, Br, Kr, and Sr, plus escape and sum peaks. Representative XRF spectra of the ABs, lung tissue, asbestos fiber, and background (area of the sample without tissue or ABs) are reported in Fig. S3 in the Supplementary Data. Elemental concentrations were calculated using the Fundamental Parameters (FP) approach (Thomsen, 2007) implemented in the

Table 1
Samples' description. The ABs count is reported per gram of dry weight of lung tissue (g_{dw}).

Case	Age	Sex	Occupation	Exposure Period (years)	Disease	ABs count / g_{dw}
A	81	M	Fibre cement Plant	27 (1962–1981)	^a AS (grade 3), ^b PP, ^c MM	$\sim 363 \cdot 10^3$
B	80	F	Fibre cement plant	> 10	AS (grade 4), PP, ^d LC	$\sim 1195 \cdot 10^3$

^a AS: Asbestosis (grading established according to Craighead et al. (Craighead et al., 1982).

^b PP: Pleural Plaques.

^c MM: Malignant Mesothelioma.

^d LC: Lung Cancer.

PyMCA software package. A reference standard (RF7-200-S2371 from AXO) containing certified concentrations of Pb, La, Pd, Mo, Cu, Fe, and Ca deposited on a 200nm-thick silicon nitride membrane, was used to check the accuracy, which resulted to be within 10 % of the expected values in the energy range $\sim 2.35 - \sim 10.54$ keV (Fig. S4 in the Supplementary Data). The limits of detection (LODs) in the working energy range can be approximately assumed to be those calculated by De Samber et al. (De Samber et al., 2018, 2016) on a bovine liver standard reference material (SRM1577c from NIST). These LODs, have a step variation in the low Z element range ($\sim 3 \cdot 10^4 - 2 \cdot 10^4$ ppm range for elements from Si to Ca), and fall in the sub-ppm range for elements from Fe to Sr (Fig. S5 in the Supplementary Data). Although the reported LODs were calculated using a similar experimental setup (same beamline, incident energy, and detector), the actual LODs may be lower because we used a 6-element detector. For small thickness values, the elemental quantification performed with FP approach was very sensitive to thickness variations. As ABs do not have constant thickness, the concentrations were calculated for regions of interest (ROI) were the thickness, which was calculated from XPChT data, did not vary more than 10 % of the average value. Considering the accuracy and the thickness variation, the error on the elemental concentrations can be assumed to be within 10 % of the calculated values. The thickness and density calculated from XPChT data in the same ROI selected for S-XRF analysis were used to define the sample matrix in the FP approach, allowing to perform a more reliable elemental quantification.

Due to the long acquisition time required by S-XRF mapping and the limited beamtime available (10 days in two experimental campaigns), it was possible to measure only nine ABs. In the following, we will focus on four representative ABs, while all nine of them were considered when calculating the average values of the elemental concentrations and mass densities.

3. Results

3.1. X-ray phase-contrast holo-tomography

The tomograms of four selected ABs are shown in Fig. 1 (projected on a plane for ease of view), and are representative of the variety of shapes that they can assume: from sheath-like to rectangular, beaded, or irregular units, more or less evenly distributed along the longitudinal axis, and often with increased size at both ends (dumbbell shape). From Fig. 1, it can be seen that tomographic data allowed clearly identifying the inner asbestos fiber and its coating, and to reveal subtle variations in their mass density. The inner fiber appears to be lacking in some sections of the ABs (e.g. Fig. 1a). The average diameter of the fibers inside the ABs felt in the range $0.2 - 0.3 \mu\text{m}$, in agreement with the median diameter of asbestos ($0.2 - 0.4 \mu\text{m}$ (Boulanger et al., 2014)). However, the fibers diameter varied even inside the same AB, sometimes exceeding that of crocidolite, amosite, and chrysotile, and reaching values as high as $0.6 \mu\text{m}$. The thickening of the inner fibers may be due to some degree of dissolution, or to accumulation of denser material around the fiber. Uncoated fibers, as the one visible in Fig. 1e and f, have diameter closer to the crocidolite standard ($0.14 - 0.19 \mu\text{m}$) (Cluff and Patitsas, 1992).

A 3D view of the tomograms of samples A1, A2, A3, and B is shown in movie files in the Supplementary Data. To appreciate fine morphological details, the movies show a full rotation around the longitudinal axis. At the end of the rotation, the external layer of the ABs (with lower density) is removed to show the inner (higher density) structure, which is highlighted by the red color.

The mass densities of the ABs calculated from XPChT data varied in the range $2.0 - 2.5 \text{ g/cm}^3$, with an average value of $2.2 \pm 0.2 \text{ g/cm}^3$ (Table S1, Supplementary Data). The density has a weak positive correlation to the relative amount of Fe. A clear correlation between the density and the thickness of the ABs is not observed,

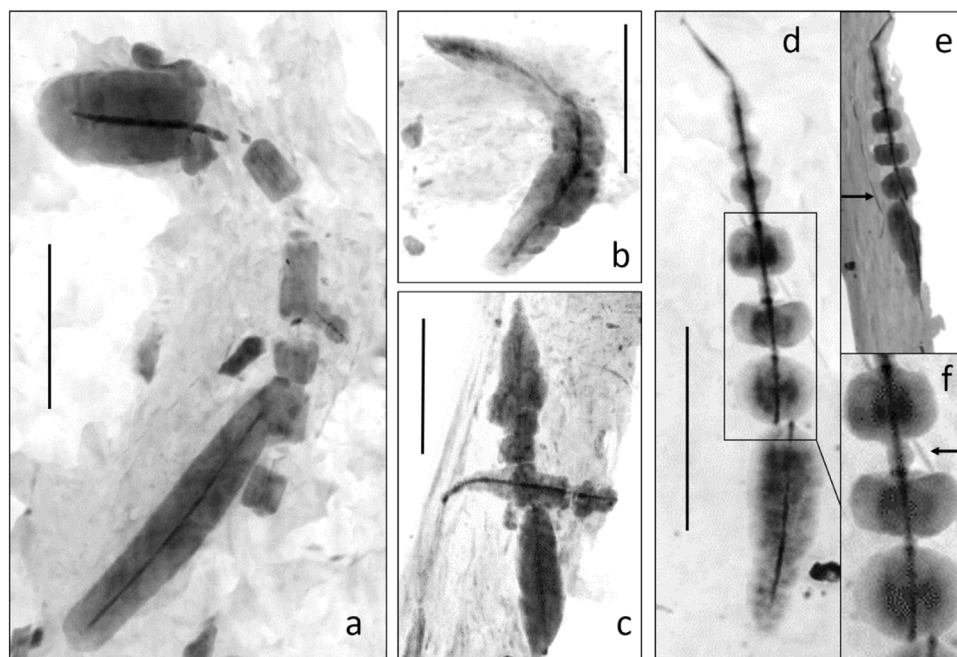


Fig. 1. Projection on a plane of the maximum grey levels of holo-tomography data. (a): sample A1; (b): sample A2; (c): sample B; (d): sample A3. The inner fiber (darker grey values) is clearly identifiable inside the ABs. The phase-contrast mode allows to image the surrounding lung tissue as well as the more absorbing ABs. A side view of sample A3 is shown in panel (e), in which the thickness of the lung tissue section ($\sim 10 \mu\text{m}$ average) and the supporting PEN film ($4 \mu\text{m}$) can be seen. Uncoated asbestos is indicated by the black arrows in panels e) (side view of panel d) and f) (magnification of the region of panel d) indicated by the rectangular box). In all images, the scale bars are $10 \mu\text{m}$ long and the pixel size is $0.07 \times 0.07 \mu\text{m}^2$.

suggesting poor correlation between the elemental composition and dimensions of the ABs. The calculated average density of the lung tissue surrounding the ABs was $1.0 \pm 0.1 \text{ g/cm}^3$ (Table S2, Supplementary Data). This value is in good agreement with the density values reported in the literature for lung tissue (1.05 g/cm^3) (Menzel et al., 2009), corroborating the densities obtained for the ABs, and giving an idea of the absolute error on the densities ($<0.1 \text{ g/cm}^3$). A representative mass density map (Sample A3) is shown in Fig. S6, along with the corresponding thickness map. The transversal profile plot of the thickness of the AB shown in Fig. S6 is bell-shaped, as expected for objects with cylindrical symmetry. On the contrary, the profile plot of the density deviates from the bell-shaped trend, revealing the presence of a denser central area corresponding to the inner asbestos fiber. This area is surrounded by less dense regions on both sides, and, moving away from the center, another dense region is detected. The density drops again approaching the rim of the AB. It is worth noting that the density map is naturally normalized by the thickness, as it derives from tomographic data.

3.2. Scanning X-ray fluorescence spectroscopy

The distribution of Fe in Samples A1, A2, A3, and B is shown in Fig. 2. It can be seen that it well mimics the shape revealed by the XPCt data collected on the very same samples (Fig. 1).

In all XRF maps, the same seventeen elements were detected: Si, P, S, Cl, K, Ca, Ti, Cr, Mn, Fe, Cu, Ni, Zn, As, Se, Br, and Sr (Figs. S7–S10 and Table S1).

The elemental quantification revealed that the major elements were Si, P, S, K, Ca, and Fe, and the minor and trace elements ($<1\%$ mass fraction) were Cl, Ti, Cr, Cu, Ni, Zn, As, Se, Br, and Sr. The mass fractions (in % for the major elements and in ppm for the minor and trace ones) are reported in the bar graphs in Fig. 3. Manganese was not quantified, because of the overlap with the strong fluorescence signal of Fe.

The corresponding numerical values are reported in Tables S1 and S2 in the Supplementary Data. The knowledge of the mass density allowed calculating the areal masses (ng/mm^2), which are also reported in Tables S1 and S2. The corresponding elemental concentrations can be derived from the areal masses and the thickness values.

All ABs ($n = 9$) analyzed had a similar structure: a well-defined border enclosing an area made of variable amounts of the same elements, which were enriched in the ABs with respect to the surrounding lung tissue. In Fig. 4, the co-localization of selected elements with Fe in sample A2 is highlighted by the purple color, which results from the color combination of Fe (red) and the other selected element (blue).

Color combination maps for major, minor, and trace elements of samples A1, A3, and B (Figs. S8–S10 in the Supplementary Data)

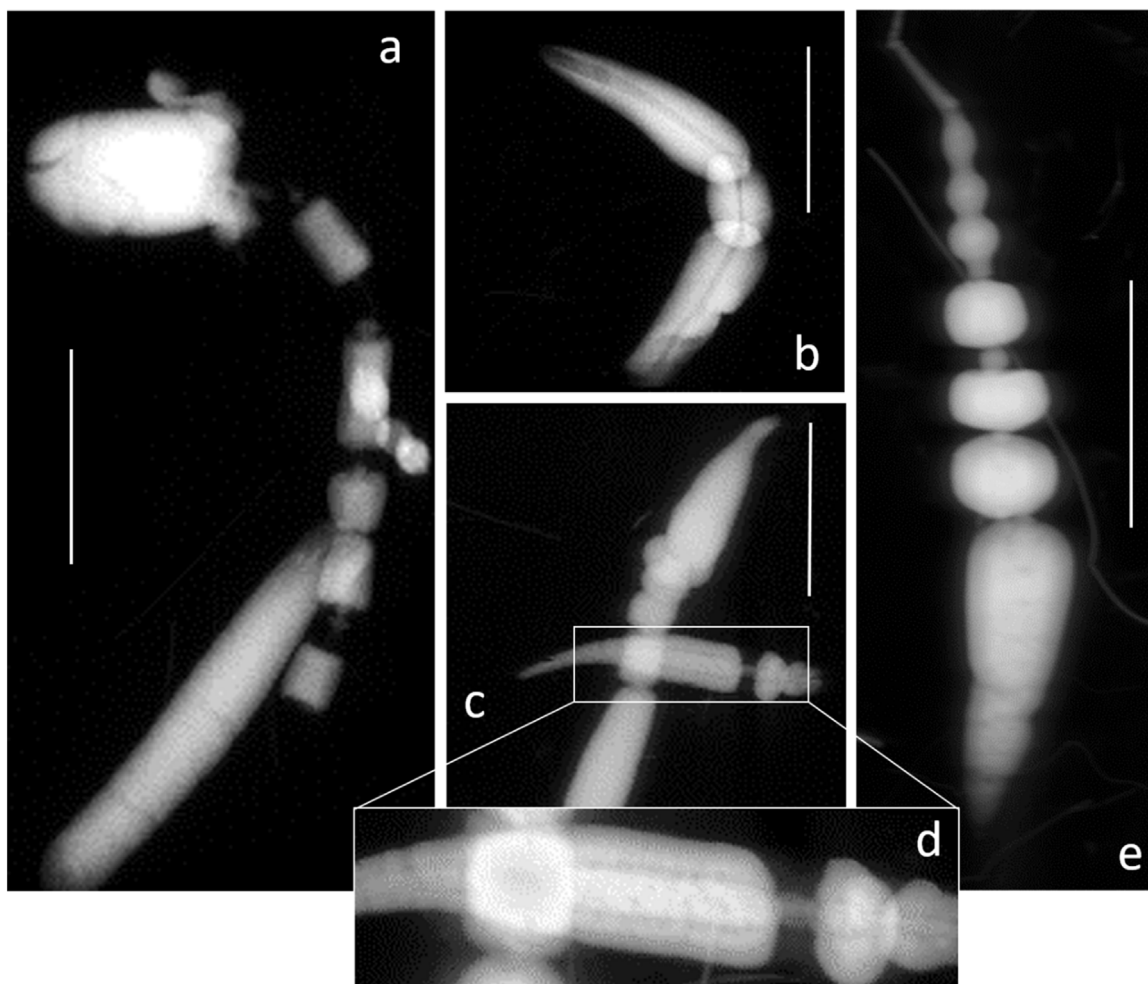


Fig. 2. Iron distribution maps of the same ABs shown in Fig. 1: (a) sample A1; (b) sample A2; (c) sample B; (e) sample A3. The distribution of Fe mimics the shape of the ABs. A complex (layered) internal structure (see text) is highlighted in the high resolution map in (d). The scale bars are $10 \mu\text{m}$ long, and the pixel size is $0.15 \times 0.15 \mu\text{m}^2$ ($0.05 \times 0.05 \mu\text{m}^2$ in panel (d)).

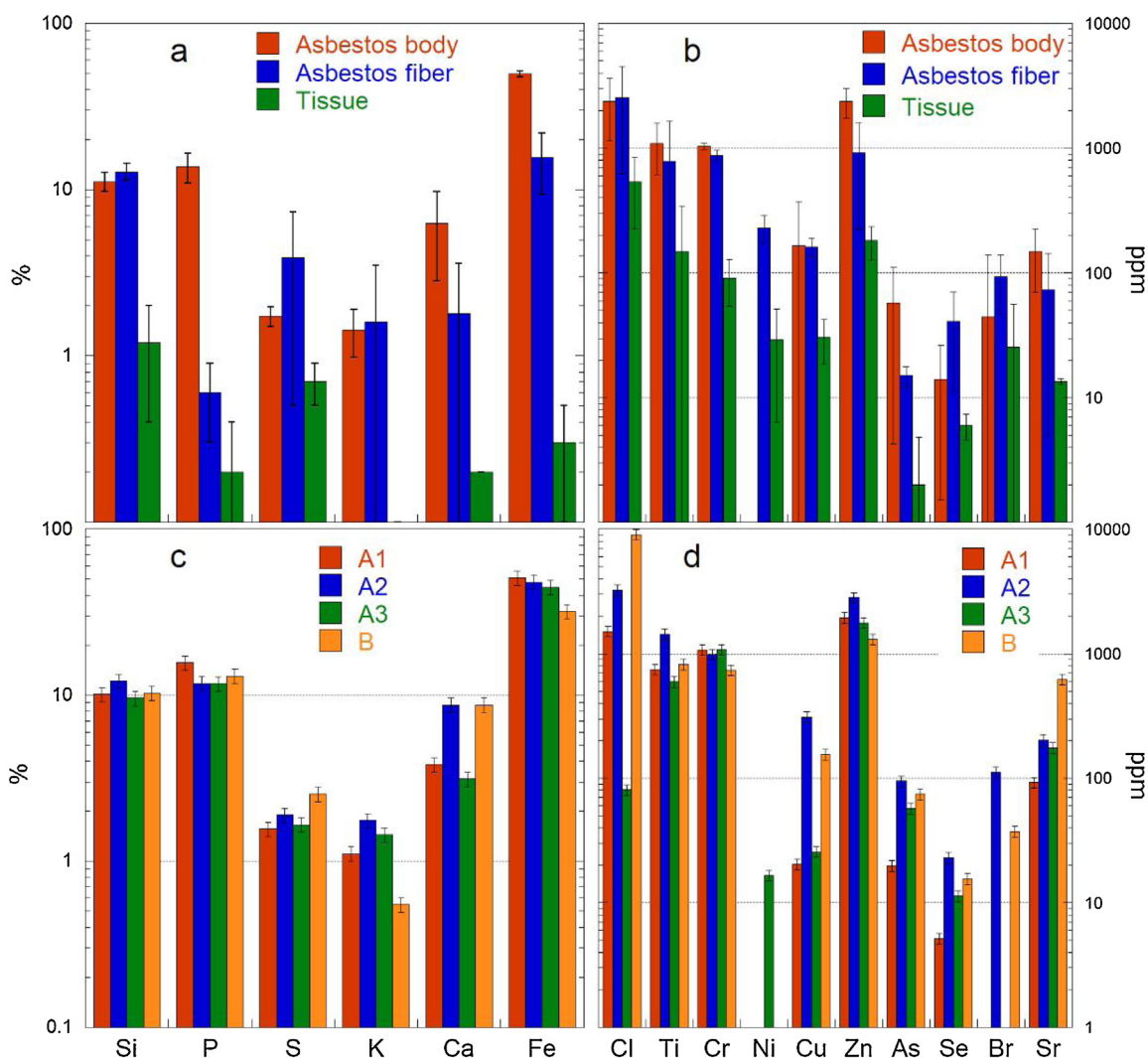


Fig. 3. Mass fractions of the major (a, c), and minor and trace (b, d) elements, calculated from XRF data. Panels (a) and (b) show the average values of the AB and lung tissue ($n = 9$). The error bars represent the relative standard deviations (RSD). Panels (c) and (d) show the mass fractions of major (c), and minor and trace (d) elements of samples A1, A2, A3, and B (Figs. 1 and 2). The error bars represent the absolute error, which was estimated to be 10 % of the reported values (see Materials and Method section). The y-axes are in logarithmic scale. The corresponding numerical values are reported in Tables S1 and S2 in the Supplementary Data, along with the areal mass values (ng/mm^2) derived from the mass fraction and density values.

reveal the co-localization with Fe of all the elements detected in the ABs. Phosphor, S, Cl, Mn, Ni, Cu, Zn, Se, As, Br, and Sr were present at lower levels also in the surrounding lung tissue, where they co-localize. Titanium and Cr were enriched in the ABs, but they are also present in the lung tissue in random spots, not co-localized with the other elements (Figs. S7–S10).

Silicon was found to occur in increased levels in the innermost area of the ABs, and at lower levels in the surrounding coating layer. The distribution of Si in the inner area of the ABs mimics the original asbestos fiber (Fig. 4, inset), which are silicate minerals. It is interesting to note that in sample A2 the innermost Si-rich area appears to be depleted of Fe and other elements (Fig. 4). Si-rich particles of 1–1.5 μm in size were detected in the lung tissue (indicated by arrows in Fig. 4).

The XRF maps also revealed a number of thinner fibers, with width varying in the range 0.15–0.35 μm . These are more evident in the distribution maps of Fe, which are shown in logarithmic (in Fig. S11, in the Supplementary Data) to enhance low intensity fluorescence signals. Some have a width of the Fe distribution larger (~ 0.8 – $1.0 \mu\text{m}$) than that expected for ideal amphibole or

chrysotile asbestos, suggesting that they may be fibers subjected to initial biomineralization process. Those with width compatible with that of uncoated asbestos fibers are composed by the same elements detected in the ABs, but with different relative mass fractions. In particular, the major elements have higher fractions of Si and S, and lower fractions of P, K, Ca, and Fe (Table S2).

4. Discussion

High resolution XPChT allowed revealing the morphology of single ABs with level of detail comparable to that of recent electron microscopy studies (Di Giuseppe et al., 2019; Gualtieri et al., 2017). However, in these studies the ABs had to be extracted from lung tissue to obtain good quality images, possibly altering them (Bardelli et al., 2017; Borelli et al., 2007; De Vuyst et al., 1998). Moreover, the width of the ABs (1–10 μm) exceeds the penetration depth of electrons ($\ll 1 \mu\text{m}$), making electron microscopies blind to internal details (unless the ABs are sectioned along the longitudinal axis, as done in the pioneering work of Pooley following a very complex and invasive sample preparation (Pooley,

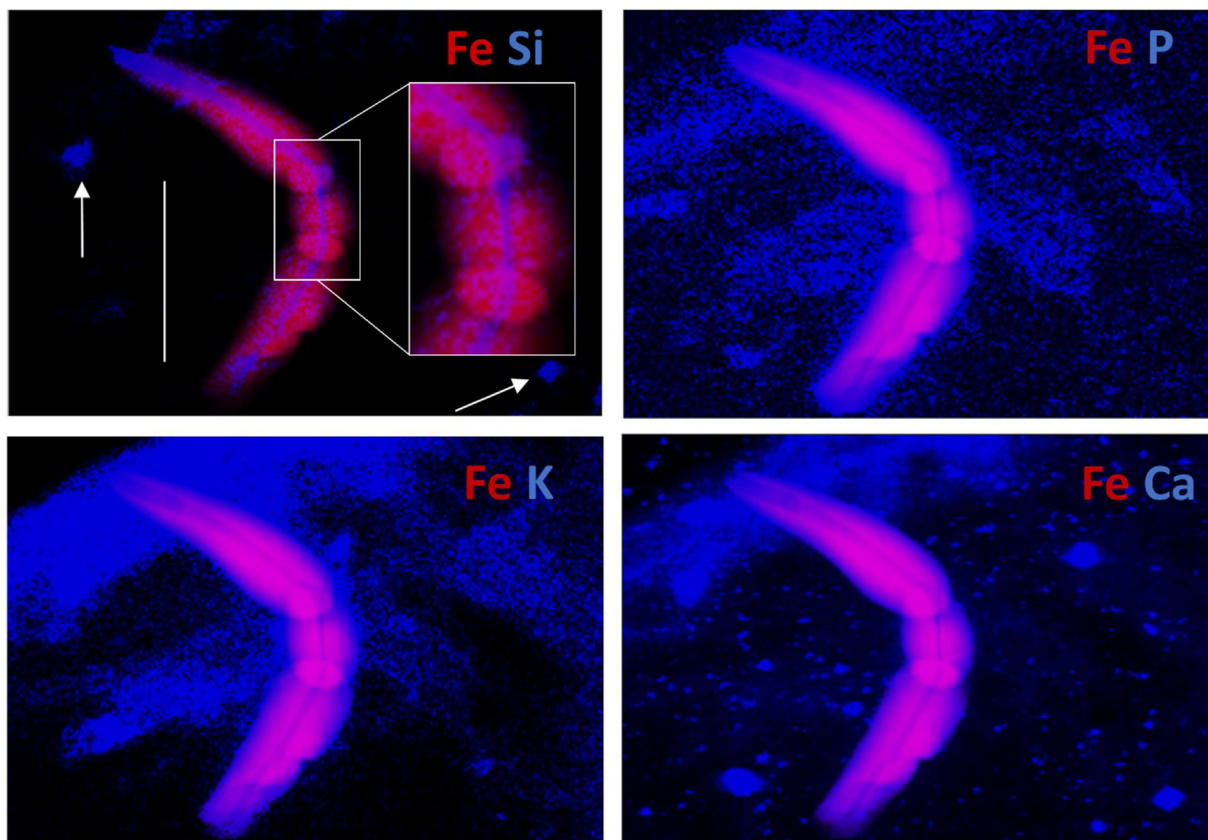


Fig. 4. XRF map of sample A2 highlighting the correlation of Fe with Si, P, K, or Ca. The distribution of Fe is shown in red color and that of the other element in blue color, so that the area where Fe is co-localized with the other element is purple-colored. The inset in the Fe-Si map shows that Si is concentrated in the inner part of the AB, where it is anti-correlated with Fe. The white arrows indicate Si-rich particles in the lung tissue (nearly 100 % in Si). Random Ca-concentrated spots in the Fe-Ca map are due to Ca contamination in the PEN membrane. The co-localization maps of Fe with the other elements are shown in Fig. S7. The vertical scale bar is 10 μm long and the pixel size is $0.15 \times 0.15 \mu\text{m}^2$.

1972)). On the contrary, hard x-rays (>1 keV) are able to penetrate several millimeters of biological tissue or support materials with similar density (paraffin, plastic, or polymer resins), making it possible to reveal the internal structure of the ABs. Another advantage is that, at the incident x-ray energies used in this work (17.05 keV), no beam damage is expected to occur, as the interaction with the samples is negligible (contrary to the electron beam used in electron microscopies). XPChT allowed obtaining quantitative information, such as the ABs mass density and thickness maps, which were used to retrieve a truly quantitative elemental quantification by S-XRF. This is a great advance with respect to our previous work (Bardelli et al., 2017), and to other works that contained only qualitative or semi-quantitative elemental analysis based on Energy Dispersive X-ray Spectroscopy coupled with scanning or transmission electron microscopy (Bursi Gandolfi et al., 2016; Di Giuseppe et al., 2019). The main limitation of this experimental approach is that the samples size is limited, because of the long acquisition time needed for fluorescence mapping (several hours) compared to the limited beamtime that it is possible to obtain at a synchrotron radiation source. In addition, as mentioned in the Materials and Method section, the experimental setup prevented detecting and quantifying elements lighter than Si, in particular, Na and Mg, which are among the main constituents of the original asbestos fibers. Besides the quantitative findings concerning the physico-chemical properties of the ABs (elemental analysis and mass density), the present work also demonstrates the potential of combined x-ray imaging and spectroscopic techniques for the study of health-threatening fibers and other particulate matter in biological tissues.

The calculated average density of the ABs was $\sim 2.2 \pm 0.3 \text{ g/cm}^3$, an intermediate value between those of ferritin and hemosiderin, which have been reported to vary the range 1.4–2.3 g/cm^3 , depending on the Fe-loading (Cook, 1929; Fankuchen, 1943). As a reference, the density of ferrihydrite, the crystalline Fe-core of ferritin is 3.8 g/cm^3 (Harrison et al., 1967), those of crocidolite, amosite, and chrysotile asbestos vary in the range 2.4–3.6 g/cm^3 (Hardy and Aust, 1995), and that of apatite, which was claimed to be present in the ABs (Bursi Gandolfi et al., 2016), is $\sim 3.2 \text{ g/cm}^3$. The average mass density of the ABs is compatible with that of highly loaded ferritin, or hemosiderin, indicating that the ABs are prevalently made of one of these Fe-storage proteins, or, most probably, of an admixture of them. Even if the presence of ferritin and hemosiderin in ABs has been proposed since long time, the first direct evidences are relatively recent (Bardelli et al., 2017; Borelli et al., 2007; Pascolo et al., 2013), and a confirmation based on their mass density was still lacking.

In agreement with FEG-SEM observations performed on animal samples (Bursi Gandolfi et al., 2016), the density distribution is compatible with a scenario in which the growth of the ABs occurs by addition of layers. These layered structures may be due to repeated attempts of the macrophages to engulf the fibers (Di Giuseppe et al., 2019). In fact, the macrophages were observed to attack the fibers preferentially from their ends (Ishida et al., 2019; Padmore et al., 2017), which would be therefore subjected to repeated coatings, explaining why ABs often have increased size at their ends.

The composition of all ABs analyzed was similar. In particular, the same elements were detected in all AB, with only minor

differences in the relative amounts of the major (Si, P, S, K, Ca, and Fe) and minor and trace (Cl, Ti, Cr, Ni, Cu, Zn, As, Se, Br, and Sr) elements. With the exception of Si, all the above elements are co-localized on the ABs, where they are enriched with respect to the surrounding lung tissue. It is reasonable to believe that, with the exception of Si, all the major elements actively take part to the biomineralization process. In fact, Fe is present in ferritin and hemosiderin, which are believed to be the main constituents of the ABs (Bardelli et al., 2017; Davis, 1964; Pooley, 1972). The observed strong correlation of Ca and P suggests that they are present as apatite or hydroxyapatite, as claimed in early works (Davis, 1964; Pooley, 1972), and recently observed by Raman spectroscopy (Bursi Gandolfi et al., 2016). Phosphor, on the other hand, may also be included in P-rich ferrihydrite (Harrison et al., 1967), and S, Cl, and K are among the most abundant minor elements in the lung tissue (Menzel et al., 2009). The observed distribution of Si reveals the asbestos fiber buried in the innermost area of the ABs. However, Si was also observed over the entire ABs area, with a concentration decreasing in the core-to-rim direction. This may indicate a possible partial dissolution of the inner fiber. Silicon-rich particles were also observed in the lung tissue, compatibly with the occupation of the workers (silica powder is a known contaminant in many industrial processes).

Possible asbestos dissolution in biological media is of interest, because the fibers constituents might migrate in the surrounding lung tissues, and eventually in the rest of the host organism, possibly playing a role in the pathogenesis of asbestos-related diseases (Bloise et al., 2016a; Gualtieri et al., 2019a; Nakamura et al., 2009). Considering the different biopersistence of amphiboles and chrysotile and that the average resident time of the fibers in the lung samples studied in this work is >10 years, it is reasonable to believe that the majority of the observed ABs formed around the more biopersistent asbestos fibers, which are indisputably the amphiboles. In fact, chrysotile was shown to undergo partial fragmentation and dissolution in three year-long in vivo animal studies (i.e. the average life expectancy of guinea pigs, mice or rats) (Bursi Gandolfi et al., 2016), and partial chrysotile dissolution was also observed in shorter time scale (weeks) by vitro studies (Bignon and Jaurand, 1983). Conversely, up to two-month in vitro leaching experiments showed a very limited dissolution (1–2 %) of crocidolite and tremolite asbestos (Andreozzi et al., 2017; Pacella et al., 2015, 2014), and recent works demonstrated the high stability of amphiboles in the biological medium (Bursi Gandolfi et al., 2016; Di Giuseppe et al., 2019; Pacella et al., 2014; Pollastri et al., 2016a), even after ~40 years of permanence in the lungs (Giacobbe et al., 2021).

Although the tissue samples studied in this work belonged to workers who have been exposed also to chrysotile asbestos, SEM-EDS measurements performed on fibers recovered after chemical digestion of the tissue showed that the prevalent fiber is crocidolite (Fig. S1). This is in agreement with the literature, as Pooley and Ranson (Pooley and Ranson, 1986) reported that only a small proportion (0.14 %, on average) of chrysotile form ABs, and Churg (Churg, 1982) observed that of 600 ABs from 82 cases, 98 % had an amphibole core, and only 2 % a chrysotile one. In general, it was also observed that the number of chrysotile fibers in the human lungs is usually lower than that of amphiboles (Friedrichs et al., 1992; Rasmuson et al., 2014), although chrysotile was more frequently used in industry. An exception is represented by the innermost area of Sample A2, which appears enriched in Si and depleted in all the other elements, especially Fe (Figs. 2, 4 and S7). This elemental distribution matches with that described in Gualtieri et al. (Gualtieri et al., 2017) and attributed to a Si-rich relict left behind after the partial dissolution of a chrysotile fiber. Therefore, it is reasonable to assume that sample A2 is an AB that

developed around a chrysotile fiber. This finding would support the scenario in which chrysotile dissolved over time, releasing major, minor, and trace elements. In fact, it has been shown by in vitro studies that chrysotile dissolution releases potentially toxic metals, such as Fe, Ni, Cr, and Mn (Gualtieri et al., 2019b; Jomova and Valko, 2011), and the amorphous Si relict left behind after its dissolution may induce both cytotoxic response and production of reactive oxygen species (ROS) (Gualtieri et al., 2019a; Turci et al., 2016). In addition, despite the Fe amount of chrysotile is ten times lower than that of the amphibole asbestos, it would become fully bio-available and highly reactive upon chrysotile dissolution (Gazzano et al., 2007; Gualtieri et al., 2019b; Turci et al., 2011).

As already pointed out, the elemental composition of the ABs revealed in this work was similar for all the ABs analyzed, suggesting a common formation mechanism, regardless of the fiber type around which they develop. This observation is in agreement with recent results showing that the pathogenicity of asbestos would be driven by a complex and subtle interplay between the structural, coordinative, and oxidative states of Fe sites at the surface of the fibers, rather than by the total bulk Fe content (Andreozzi et al., 2017; Pacella et al., 2015). This mechanism would be common to all asbestos, and may be assumed to be the basic mechanism of the initial formation of the ABs, which would explain the similar composition observed in this work for all ABs.

Finally, in all the ABs analyzed, the Fe content resulted to be higher (32–51 %, Table S1) than that contained in chrysotile (0.1–0.4 % (Pollastri et al., 2016b)) and/or crocidolite asbestos (~20 % (Pacella et al., 2019)). This finding opens two opposite scenarios: in the first, the Fe that take part to the formation of the ABs originates from the fiber's bulk, and progressively concentrates on its surface as long as the fiber dissolves; in the second, the Fe that take part to the formation of the ABs is endogenous (i.e., derives from the host organism Fe-pool). Further experimental work is needed to answer this question, as the first hypothesis is supported by the fiber dissolution mechanisms and Fe re-precipitation highlighted by Pacella et al. (2015) and Andreozzi et al. (2017), but nonetheless the second hypothesis cannot be excluded in light of the results recently obtained on erionite fibers, which do not contain Fe in their composition, by Ballirano and Pacella (2016), and Pacella et al. (2017).

Funding

This research was funded by the Marie Skłodowska-Curie Individual Fellowship action BiominAB-3D (GA-707905 - H2020).

Declaration of Competing Interest

The authors declare that they have no known competing financial interests or personal relationships that could have appeared to influence the work reported in this paper.

Acknowledgements

We are grateful to the ID16A-NI beamline staff at the ESRF, and in particular to Sylvain Bohic, Alexandra Pacureanu, and Murielle Salomé, for assistance and useful discussion during and after x-ray tomography and x-ray fluorescence spectroscopy measurements. We thank ESRF for granting beamtime through experiments LS-2548 and LS-2694. This work has received approval for research ethics from the bioethical committees of the University of Torino and Martini hospital (Turin). A proof/certificate of approval is available upon request. The authors declare no competing interests.

Appendix A. Supplementary data

Supplementary material related to this article can be found, in the online version, at doi:<https://doi.org/10.1016/j.toxlet.2021.05.002>.

References

- Abdel-Rahman, O., 2018. Global trends in mortality from malignant mesothelioma: analysis of WHO mortality database (1994–2013). *Clin. Respir. J.* 12, 2090–2100. doi:<http://dx.doi.org/10.1111/crj.12778>.
- Andreozzi, G.B., Pacella, A., Corazzari, I., Tomatis, M., Turci, F., 2017. Surface reactivity of amphibole asbestos: a comparison between crocidolite and tremolite. *Sci. Rep.* 7, 1–9. doi:<http://dx.doi.org/10.1038/s41598-017-14480-z>.
- Ballirano, P., Pacella, A., 2016. Erionite-Na upon heating: dehydration dynamics and exchangeable cations mobility. *Sci. Rep.* 6, 1–8. doi:<http://dx.doi.org/10.1038/srep22786>.
- Bardelli, F., Veronesi, G., Capella, S., Bellis, D., Charlet, L., Cedola, A., Belluso, E., 2017. New insights on the biomineralisation process developing in human lungs around inhaled asbestos fibres. *Sci. Rep.* 7, 1–11. doi:<http://dx.doi.org/10.1038/srep44862>.
- Barrett, J.C., Lamb, P.W., Wiseman, R.W., 1989. Multiple mechanisms for the carcinogenic effects of asbestos and other mineral fibers. *Environ. Health Perspect.* doi:<http://dx.doi.org/10.1289/ehp.898181>.
- Belluso, E., Bellis, D., Fornero, E., Capella, S., Ferraris, G., Coverlizza, S., 2006. Assessment of inorganic fibre burden in biological samples by scanning Electron microscopy – energy dispersive spectroscopy. *Microchim. Acta* 155, 95–100. doi:<http://dx.doi.org/10.1007/s00604-006-0524-y>.
- Bianchi, C., Bianchi, T., 2014. Global mesothelioma epidemic: trend and features. *Indian J. Occup. Environ. Med.* 18, 82–88. doi:<http://dx.doi.org/10.4103/0019-5278.146897>.
- Bigon, J., Jaurand, M.C., 1983. Biological in vitro and in vivo responses of chrysotile versus amphiboles. *Environ. Health Perspect.* 51, 73–80. doi:<http://dx.doi.org/10.2307/3429731>.
- Bloise, A., Barca, D., Gualtieri, A.F., Pollastri, S., Belluso, E., 2016a. Trace elements in hazardous mineral fibres. *Environ. Pollut.* 216, 314–323. doi:<http://dx.doi.org/10.1016/j.envpol.2016.06.007>.
- Bloise, A., Punturo, R., Catalano, M., Miriello, D., Cirrincione, R., 2016b. Naturally occurring asbestos (NOA) in rock and soil and relation with human activities: the monitoring example of selected sites in Calabria (southern Italy). *Ital. J. Geosci.* 135, 268–279. doi:<http://dx.doi.org/10.3301/IJG.2015.24>.
- Borelli, V., Brochetta, C., Melato, M., Rizzardi, C., Polentarutti, M., Busatto, C., Vita, F., Abbate, R., Gotter, R., Zabuuchi, G., 2007. A procedure for the isolation of asbestos bodies from lung tissue by exploiting their magnetic properties: a new approach to asbestos body study. *J. Toxicol. Environ. Health A* 70, 1232–1240. doi:<http://dx.doi.org/10.1080/15287390701380906>.
- Boulanger, G., Andujar, P., Paireon, J.C., Billon-Galland, M.A., Dion, C., Dumortier, P., Brochard, P., Sobaszek, A., Bartsch, P., Paris, C., Jaurand, M.C., 2014. Quantification of short and long asbestos fibers to assess asbestos exposure: a review of fiber size toxicity. *Environ. Health A Glob. Access Sci. Source* doi:<http://dx.doi.org/10.1186/1476-069X-13-59>.
- Bursi Gandolfi, N., Gualtieri, A.F., Pollastri, S., Tibaldi, E., Belpoggi, F., 2016. Assessment of asbestos body formation by high resolution FEG-SEM after exposure of Sprague-Dawley rats to chrysotile, crocidolite, or erionite. *J. Hazard. Mater.* 306, 95–104. doi:<http://dx.doi.org/10.1016/j.jhazmat.2015.11.050>.
- Capella, S., Bellis, D., Fioretti, E., Marinelli, R., Belluso, E., 2020. Respirable inorganic fibers dispersed in air and settled in human lung samples: assessment of their nature, source, and concentration in a NW Italy large city. *Environ. Pollut.* 263, 114384. doi:<http://dx.doi.org/10.1016/j.envpol.2020.114384>.
- Carbone, M., Ly, B.H., Dodson, R.F., Pagano, I., Morris, P.T., Dogan, U.A., Gazdar, A.F., Pass, H.I., Yang, H., 2012. Malignant mesothelioma: facts, myths, and hypotheses. *J. Cell. Physiol.* doi:<http://dx.doi.org/10.1002/jcp.22724>.
- Carbone, M., Adusumilli, P.S., Alexander, H.R., Baas, P., Bardelli, F., Bononi, A., Bueno, R., Felley-Bosco, E., Galateau-Salle, F., Jablons, D., Mansfield, A.S., Minaai, M., Perrot, M., Pesavento, P., Rusch, V., Severson, D.T., Taioli, E., Tsao, A., Woodard, G., Yang, H., Zauderer, M.G., Pass, H.I., 2019. Mesothelioma: scientific clues for prevention, diagnosis, and therapy. *CA Cancer J. Clin.* 69, 402–429. doi:<http://dx.doi.org/10.3322/caac.21572>.
- Cesar da Silva, J., Pacureanu, A., Yang, Y., Bohic, S., Morawe, C., Barrett, R., Cloetens, P., 2017. Efficient concentration of high-energy x-rays for diffraction-limited imaging resolution. *Optica* 4, 492. doi:<http://dx.doi.org/10.1364/optica.4.000492>.
- Churg, A., 1982. Fiber counting and analysis in the diagnosis of asbestos-related disease. *Hum. Pathol.* 13, 381–392. doi:[http://dx.doi.org/10.1016/S0046-8177\(82\)80227-X](http://dx.doi.org/10.1016/S0046-8177(82)80227-X).
- Churg, A.M., Warnock, M.L., 1981. Asbestos and other ferruginous bodies: their formation and clinical significance. *Am. J. Pathol.* 102, 447–456.
- Cloetens, P., Ludwig, W., Baruchel, J., Guigay, J.P., Pernot-Rejmánková, P., Salomé-Pateyron, M., Schlenker, M., Buffière, J.Y., Maire, E., Peix, G., 1999. Hard X-ray phase imaging using simple propagation of a coherent synchrotron radiation beam. *J. Phys. D Appl. Phys.* 32. doi:<http://dx.doi.org/10.1088/0022-3727/32/10A/330>.
- Cluff, D.L., Patitsas, A.J., 1992. Size characterization of asbestos fibers by means of electrostatic alignment and light-scattering techniques. *Aerosol Sci. Technol.* 17, 186–198. doi:<http://dx.doi.org/10.1080/02786829208959570>.
- Cook, F., 1929. The structure and composition of hemosiderin. *J. Biol. Chem.* 82, 595–609.
- Craighead, J.E., Abraham, J.L., Churg, A., Green, F.H., Kleinerman, J., Pratt, P.C., Seemayer, T.A., Vallyathan, V., Weill, H., 1982. The pathology of asbestos-associated diseases of the lungs and pleural cavities: diagnostic criteria and proposed grading schema. Report of the Pneumoconiosis Committee of the College of American Pathologists and the National Institute for Occupational Sa. *Arch. Pathol. Lab. Med.* 106, 544–596.
- Davis, J.M., 1964. The ultrastructure of asbestos bodies from human lung. *Br. J. Exp. Pathol.* 45, 642–646.
- De Samber, B., Niemiec, M.J., Laforce, B., Garrevoet, J., Vergucht, E., De Rycke, R., Cloetens, P., Urban, C.F., Vincze, L., 2016. Probing intracellular element concentration changes during neutrophil extracellular trap formation using synchrotron radiation based X-ray fluorescence. *PLoS One* 11, e0165604. doi:<http://dx.doi.org/10.1371/journal.pone.0165604>.
- De Samber, B., Meul, E., Laforce, B., De Paepe, B., Smet, J., De Bruyne, M., De Rycke, R., Bohic, S., Cloetens, P., Van Coster, R., Vandennebelee, P., Berghe, T., Vandenberghe, P., 2018. Nanoscopic X-ray fluorescence imaging and quantification of intracellular key-elements in cryofrozen Friedreich's ataxia fibroblasts. *PLoS One* 13, 1–24. doi:<http://dx.doi.org/10.1371/journal.pone.0190495>.
- De Vuyst, P., Karjalainen, A., Dumortier, P., Paireon, J.C., Monsó, E., Brochard, P., Teschler, H., Tossavainen, A., Gibbs, A., 1998. Guidelines for mineral fibre analyses in biological samples: report of the ERS Working Group. *Eur. Respir. J.* 11, 1416–1426.
- Di Giuseppe, D., Zoboli, A., Vigliaturo, R., Gieré, R., Bonasoni, M.P., Sala, O., Gualtieri, A.F., 2019. Mineral fibres and asbestos bodies in human lung tissue: a case study. *Minerals* 9, 1–21. doi:<http://dx.doi.org/10.3390/min9100618>.
- Fankuchen, I., 1943. V. X-ray diffraction data on ferritin and apoferritin. *J. Biol. Chem.* 150, 57–59.
- Fantauzzi, M., Pacella, A., Fournier, J., Gianfagna, A., Andreozzi, G.B., Rossi, A., 2012. Surface chemistry and surface reactivity of fibrous amphiboles that are not regulated as asbestos. *Anal. Bioanal. Chem.* 404, 821–833. doi:<http://dx.doi.org/10.1007/s00216-012-6190-5>.
- Friedrichs, K.H., Brockmann, M., Fischer, M., Wick, G., 1992. Electron microscopy analysis of mineral fibers in human lung tissue. *Am. J. Ind. Med.* 22, 49–58. doi:<http://dx.doi.org/10.1002/ajim.4700220105>.
- Fubini, B., Mollo, L., 1995. Role of iron in the reactivity of mineral fibers. *Toxicol. Lett.* 82–83, 951–960.
- Gawda, A., Majka, G., Nowak, B., Śróttek, M., Walczewska, M., Marcinkiewicz, J., 2018. Air particulate matter SRM 1648a primes macrophages to hyperinflammatory response after LPS stimulation. *Inflamm. Res.* 67, 765–776. doi:<http://dx.doi.org/10.1007/s00011-018-1165-4>.
- Gazzano, E., Turci, F., Foresti, E., Putzu, M.G., Aldieri, E., Silvagno, F., Lesci, I.G., Tomatis, M., Riganti, C., Romano, C., Fubini, B., Roveri, N., Chigo, D., 2007. Iron-loaded synthetic chrysotile: a new model solid for studying the role of iron in asbestos toxicity. *Chem. Res. Toxicol.* 20, 380–387. doi:<http://dx.doi.org/10.1021/tx600354f>.
- Ghio, A.J., LeFurgey, A., Roggli, V.L., 1997. In vivo accumulation of iron on crocidolite is associated with decrements in oxidant generation by the fiber. *J. Toxicol. Environ. Health* 50, 125–142. doi:<http://dx.doi.org/10.1080/009841097160537>.
- Ghio, A.J., Stonehuerner, J., Richards, J., Devlin, R.B., 2008. Iron homeostasis in the lung following asbestos exposure. *Antioxid. Redox Signal.* 10, 371–377. doi:<http://dx.doi.org/10.1089/ars.2007.1909>.
- Giacobbe, C., Di Giuseppe, D., Zoboli, A., Lassinantti Gualtieri, M., Bonasoni, P., Moliterni, A., Corriero, N., Altomare, A., Wright, J., Gualtieri, A.F., 2021. Crystal structure determination of a lifelong biopersistent asbestos fibre using single-crystal synchrotron X-ray micro-diffraction. *IUCr* 8, 76–86. doi:<http://dx.doi.org/10.1107/s2052252520015079>.
- Gianoncelli, A., Kourousias, G., Pascolo, L., Rizzardi, C., Ceccone, G., Kaulich, B., Kiskinova, M., 2013. Life science applications and research potential of the TwinMic spectromicroscopy station at ELETTRA. *J. Phys. Conf. Ser.* 463, 012004. doi:<http://dx.doi.org/10.1088/1742-6596/463/1/012004>.
- Gloyne, S.R., 1929. The presence of the asbestos body in the lesions of asbestos workers. *Tubercle* 10, 404.
- Gloyne, S.R., 1931a. The formation of the asbestos body in the lung. *Tubercle* 12, 339.
- Gloyne, S.R., 1931b. The formation of the asbestosis body in the lung. *Tubercle* 12, 399–401. doi:[http://dx.doi.org/10.1016/S0041-3879\(31\)80143-6](http://dx.doi.org/10.1016/S0041-3879(31)80143-6).
- Governa, M., Amati, M., 1999. Role of iron in Asbestos-Body-induced oxidant radical generation. *J. Toxicol. Environ. Health Part A* 58, 279–287. doi:<http://dx.doi.org/10.1080/009841099157241>.
- Gramaccioni, C., Yang, Y., Pacureanu, A., Viganò, N., Procopio, A., Valenti, P., Rosa, L., Berlutti, F., Bohic, S., Cloetens, P., 2020. Cryo-nanoimaging of single human macrophage cells: 3D structural and chemical quantification. *Anal. Chem.* 92, 4814–4819. doi:<http://dx.doi.org/10.1021/acs.analchem.9b04096>.
- Gualtieri, A.F., Bursi Gandolfi, N., Pollastri, S., Burghammer, M., Tibaldi, E., Belpoggi, F., Pollak, K., Langenhorst, F., Vigliaturo, R., Dražić, G., 2017. New insights into the toxicity of mineral fibres: a combined in situ synchrotron μ -XRD and HR-TEM study of chrysotile, crocidolite, and erionite fibres found in the tissues of Sprague-Dawley rats. *Toxicol. Lett.* 274, 20–30. doi:<http://dx.doi.org/10.1016/j.toxlet.2017.04.004>.

- Gualtieri, A.F., Lusvardi, G., Pedone, A., Di Giuseppe, D., Zoboli, A., Mucci, A., Zambon, A., Filaferro, M., Vitale, G., Benassi, M., Avallone, R., Pasquali, L., Lassinantti Gualtieri, M., 2019a. Structure model and toxicity of the product of biodegradation of chrysotile asbestos in the lungs. *Chem. Res. Toxicol.* 32, 2063–2077. doi:<http://dx.doi.org/10.1021/acs.chemrestox.9b00220>.
- Gualtieri, A.F., Lusvardi, G., Zoboli, A., Di Giuseppe, D., Lassinantti Gualtieri, M., 2019b. Biodurability and release of metals during the dissolution of chrysotile, crocidolite and fibrous erionite. *Environ. Res.* 171, 550–557. doi:<http://dx.doi.org/10.1016/j.envres.2019.01.011>.
- Guinier, A., 1994. X-Ray Diffraction: In Crystals, Imperfect Crystals, and Amorphous Bodies (Dover Books on Physics). Dover Publications.
- Hardy, J.A., Aust, A.E., 1995. The effect of iron binding on the ability of crocidolite asbestos to catalyze DNA single-strand breaks. *Carcinogenesis* 16, 319–325.
- Harrison, P.M., Fischbach, F.A., Hoy, T.G., Haggis, G.H., 1967. Ferric oxyhydroxide core of ferritin. *Nature* 216, 1188–1190. doi:<http://dx.doi.org/10.1038/2161188a0>.
- Hwang, C.Y., Gibbs, G.W., 1981. The dimensions of airborne asbestos fibres - I. Crocidolite from Kuruman area, Cape Province, South Africa. *Ann. Occup. Hyg.* 24, 23–41. doi:<http://dx.doi.org/10.1093/annhyg/24.1.23>.
- Ishida, T., Fujihara, N., Nishimura, T., Funabashi, H., Hirota, R., Ikeda, T., Kuroda, A., 2019. Live-cell imaging of macrophage phagocytosis of asbestos fibers under fluorescence microscopy. *Genes Environ.* 41 doi:<http://dx.doi.org/10.1186/s41021-019-0129-4>.
- Jomova, K., Valko, M., 2011. Advances in metal-induced oxidative stress and human disease. *Toxicology* doi:<http://dx.doi.org/10.1016/j.tox.2011.03.001>.
- Jones, R.N., Hughes, J.M., Weill, H., 1996. Asbestos exposure, asbestosis, and asbestos-attributable lung cancer. *Thorax* 51, 9–15. doi:http://dx.doi.org/10.1136/thx.51.suppl_2.s9.
- Kameda, T., Takahashi, K., Kim, R., Jiang, Y., Movahed, M., Park, E.-K., Rantanen, J., 2014. Asbestos: use, bans and disease burden in Europe. *Bull. World Health Organ.* 92, 790–797. doi:<http://dx.doi.org/10.2471/BLT.13.132118>.
- Khimchenko, A., Bikis, C., Pacureanu, A., Hieber, S.E., Thalmann, P., Deyhle, H., Schweighauser, G., Hench, J., Frank, S., Müller-Gerbl, M., Schulz, G., Cloetens, P., Müller, B., 2018. Hard X-ray nanoholotomography: large-scale, label-free, 3D neuroimaging beyond optical limit. *Adv. Sci.* 5, 1–9. doi:<http://dx.doi.org/10.1002/adv.201700694>.
- Klebe, S., Leigh, J., Henderson, D.W., Nurminen, M., 2020. Asbestos, smoking and lung cancer: an update. *Int. J. Environ. Res. Public Health* doi:<http://dx.doi.org/10.3390/ijerph17010258>.
- Lund, L.G., Williams, M.G., Dodson, R.F., Aust, A.E., 1994. Iron associated with asbestos bodies is responsible for the formation of single strand breaks in phi X174 RFI DNA. *Occup. Environ. Med.* 51, 200–204. doi:<http://dx.doi.org/10.1136/oem.51.3.200>.
- Mace, M.L., McLemore, T.L., Roggli, V., Brinkley, B.R., Greenberg, S.D., 1980. Scanning electron microscopic examination of human asbestos bodies. *Cancer Lett.* 9, 95–104.
- Mazurek, J.M., Syamlal, G., Wood, J.M., Hendricks, S.A., Weston, A., 2017. Malignant mesothelioma mortality – United States, 1999–2015. *MMWR Morb. Mortal. Wkly. Rep.* 66, 214–218. doi:<http://dx.doi.org/10.15585/mmwr.mm6608a3>.
- McLemore, T.L., Mace, M.L., Roggli, V., Marshall, M.V., Lawrence, E.C., Wilson, R.K., Martin, R.R., Brinkley, B.R., Greenberg, S.D., 1980. Asbestos body phagocytosis by human free alveolar macrophages. *Cancer Lett.* 9, 85–93.
- Menzel, H., Clement, C., DeLuca, P., 2009. Adult reference computational phantoms. *Ann. ICRP* doi:<http://dx.doi.org/10.1016/j.icrp.2009.09.001>.
- Nakamura, E., Makishima, A., Hagino, K., Okabe, K., 2009. Accumulation of radium in ferruginous protein bodies formed in lung tissue: association of resulting radiation hotspots with malignant mesothelioma and other malignancies. *Proc. Jpn. Acad. Ser. B* 85, 229–239. doi:<http://dx.doi.org/10.2183/pjab.85.229>.
- Noonan, C.W., 2017. Environmental asbestos exposure and risk of mesothelioma. *Ann. Transl. Med.* doi:<http://dx.doi.org/10.21037/atm.2017.03.74>.
- Pacella, A., Andreozzi, G.B., Fournier, J., 2010. Detailed crystal chemistry and iron topochemistry of asbestos occurring in its natural setting: a first step to understanding its chemical reactivity. *Chem. Geol.* 277, 197–206. doi:<http://dx.doi.org/10.1016/j.chemgeo.2010.07.018>.
- Pacella, A., Andreozzi, G.B., Fournier, J., Stievano, L., Giantomassi, F., Lucarini, G., Rippo, M.R., Pugnali, A., 2012. Iron topochemistry and surface reactivity of amphibole asbestos: relations with in vitro toxicity. *Anal. Bioanal. Chem.* 402, 871–881. doi:<http://dx.doi.org/10.1007/s00216-011-5525-y>.
- Pacella, A., Fantauzzi, M., Turci, F., Creminini, C., Montoreali, M.R., Nardi, E., Atzei, D., Rossi, A., Andreozzi, G.B., 2014. Dissolution reaction and surface iron speciation of UICC crocidolite in buffered solution at pH 7.4: a combined ICP-OES, XPS and TEM investigation. *Geochim. Cosmochim. Acta* 127, 221–232. doi:<http://dx.doi.org/10.1016/j.gca.2013.11.035>.
- Pacella, A., Fantauzzi, M., Turci, F., Creminini, C., Montoreali, M.R., Nardi, E., Atzei, D., Rossi, A., Andreozzi, G.B., 2015. Surface alteration mechanism and topochemistry of iron in tremolite asbestos: a step toward understanding the potential hazard of amphibole asbestos. *Chem. Geol.* 405, 28–38. doi:<http://dx.doi.org/10.1016/j.chemgeo.2015.03.028>.
- Pacella, A., Creminini, C., Nardi, E., Montoreali, M.R., Pettiti, I., Ballirano, P., 2017. The mechanism of iron binding processes in erionite fibres. *Sci. Rep.* 7, 1–8. doi:<http://dx.doi.org/10.1038/s41598-017-01477-x>.
- Pacella, A., Andreozzi, G.B., Nodari, L., Ballirano, P., 2019. Chemical and structural characterization of UICC crocidolite fibres from Koegas Mine, Northern Cape (South Africa). *Period. di Mineral.* 88, 297–306. doi:<http://dx.doi.org/10.2451/2019PM910>.
- Padmore, T., Stark, C., Turkevich, L.A., Champion, J.A., 2017. Quantitative analysis of the role of fiber length on phagocytosis and inflammatory response by alveolar macrophages. *Biochim. Biophys. Acta - Gen. Subj.* 1861, 58–67. doi:<http://dx.doi.org/10.1016/j.bbagen.2016.09.031>.
- Park, E.K., Takahashi, K., Hoshuyama, T., Cheng, T.J., Delgermaa, V., Le, G.V., Sorahan, T., 2011. Global magnitude of reported and unreported mesothelioma. *Environ. Health Perspect.* 119, 514–518. doi:<http://dx.doi.org/10.1289/ehp.1002845>.
- Pascolo, L., Gianoncelli, A., Kaulich, B., Rizzardi, C., Schneider, M., Bottin, C., Polentarutti, M., Kiskinova, M., Longoni, A., Melato, M., 2011. Synchrotron soft X-ray imaging and fluorescence microscopy reveal novel features of asbestos body morphology and composition in human lung tissues. *Part. Fibre Toxicol.* 8, 7. doi:<http://dx.doi.org/10.1186/1743-8977-8-7>.
- Pascolo, L., Gianoncelli, A., Schneider, G., Salomé, M., Schneider, M., Calligaro, C., Kiskinova, M., Melato, M., Rizzardi, C., 2013. The interaction of asbestos and iron in lung tissue revealed by synchrotron-based scanning X-ray microscopy. *Sci. Rep.* 3, 1123. doi:<http://dx.doi.org/10.1038/srep01123>.
- Pollastri, S., Gualtieri, A.F., Vigliaturo, R., Ignatyev, K., Strafella, E., Pugnali, A., Croce, A., 2016a. Stability of mineral fibres in contact with human cell cultures. An in situ XANES, m XRD and XRF iron mapping study. *Chemosphere* 164, 547–557. doi:<http://dx.doi.org/10.1016/j.chemosphere.2016.08.139>.
- Pollastri, S., Perchiazi, N., Lezzerini, M., Plaisier, J.R., Cavallo, A., Dalconi, M.C., Gandolfi, N.B., Gualtieri, A.F., 2016b. The crystal structure of mineral fibres. 1. Chrysotile. *Period. di Miner.* 85, 249–259. doi:<http://dx.doi.org/10.2451/2016PM655>.
- Pooley, F.D., 1972. Asbestos bodies, their formation, composition and character. *Environ. Res.* 5, 363–379.
- Pooley, F.D., Ranson, D.L., 1986. Comparison of the results of asbestos fibre dust counts in lung tissue obtained by analytical electron microscopy and light microscopy. *J. Clin. Pathol.* 39, 313–317. doi:<http://dx.doi.org/10.1136/jcp.39.3.313>.
- Rasmuson, J.O., Roggli, V.L., Boelter, F.W., Rasmuson, E.J., Redinger, C.F., 2014. Cumulative Retrospective Exposure Assessment (REA) as a predictor of amphibole asbestos lung burden: validation procedures and results for industrial hygiene and pathology estimates. *Inhal. Toxicol.* 26, 1–13. doi:<http://dx.doi.org/10.3109/08958378.2013.845273>.
- Reid, A., De Klerk, N.H., Magnani, C., Ferrante, D., Berry, G., Musk, A.W., Merler, E., 2014. Mesothelioma risk after 40 years since first exposure to asbestos: a pooled analysis. *Thorax* 69, 843–850. doi:<http://dx.doi.org/10.1136/thoraxjnl-2013-204161>.
- Schneider, C.A., Rasband, W.S., Eliceiri, K.W., 2012. NIH Image to ImageJ: 25 years of image analysis. *Nat. Methods* doi:<http://dx.doi.org/10.1038/nmeth.2089>.
- Solé, V.A., Papillon, E., Cotte, M., Walter, P., Susini, J., 2007. A multiplatform code for the analysis of energy-dispersive X-ray fluorescence spectra. *Spectrochim. Acta Part B At. Spectrosc.* 62, 63–68. doi:<http://dx.doi.org/10.1016/j.sab.2006.12.002>.
- Spurny, K.R., 1989. On the release of asbestos fibers from weathered and corroded asbestos cement products. *Environ. Res.* 48, 100–116. doi:[http://dx.doi.org/10.1016/S0013-9351\(89\)80089-1](http://dx.doi.org/10.1016/S0013-9351(89)80089-1).
- Suzuki, Y., Churg, J., 1969. Structure and development of the asbestos body. *Am. J. Pathol.* 55, 79–107.
- Thomsen, V., 2007. X-Ray Fluorescence, 22. , pp. 46–50.
- Toyokuni, S., 2014. Iron overload as a major targetable pathogenesis of asbestos-induced mesothelial carcinogenesis. *Redox Rep.* 19, 1–7. doi:<http://dx.doi.org/10.1179/1351000213y.0000000075>.
- Turci, F., Tomatis, M., Lesci, I.G., Roveri, N., Fubini, B., 2011. The iron-related molecular toxicity mechanism of synthetic asbestos nanofibres: a model study for high-aspect-ratio nanoparticles. *Chem. - A Eur. J.* 17, 350–358. doi:<http://dx.doi.org/10.1002/chem.201001893>.
- Turci, F., Pavan, C., Leinardi, R., Tomatis, M., Pastore, L., Garry, D., Anguissola, S., Lison, D., Fubini, B., 2016. Revisiting the paradigm of silica pathogenicity with synthetic quartz crystals: the role of crystallinity and surface disorder. *Part. Fibre Toxicol.* 13 doi:<http://dx.doi.org/10.1186/s12989-016-0136-6>.
- Uguen, M., Dewitte, J.-D., Marcorelles, P., Loddé, B., Pougnet, R., Saliou, P., De Braekeleer, M., Uguen, A., 2017. Asbestos-related lung cancers: a retrospective clinical and pathological study. *Mol. Clin. Oncol.* 7, 135–139. doi:<http://dx.doi.org/10.3892/mco.2017.1277>.
- Wagner, J.C., Sleggs, C.A., Marchand, P., 1960. Diffuse pleural mesothelioma and asbestos exposure in the North Western Cape Province. *Br. J. Ind. Med.* 17, 260–271. doi:<http://dx.doi.org/10.1136/oem.17.4.260>.
- Wagner, J.C., Berry, G., Skidmore, J.W., Timbrell, V., 1974. The effects of the inhalation of asbestos in rats. *Br. J. Cancer* 29, 252–269. doi:<http://dx.doi.org/10.1038/bjc.1974.65>.
- Yang, H., Bocchetta, M., Kroczyńska, B., Elmishad, A.G., Chen, Y., Liu, Z., Bubicic, C., Mossman, B.T., Pass, H.I., Testa, J.R., Franzoso, G., Carbone, M., 2006. TNF- α inhibits asbestos-induced cytotoxicity via a NF- κ B-dependent pathway: a possible mechanism for asbestos-induced oncogenesis. *Proc. Natl. Acad. Sci. U. S. A.* 103, 10397–10402. doi:<http://dx.doi.org/10.1073/pnas.0604008103>.
- Yang, H., Rivera, Z., Jube, S., Nasu, M., Bertino, P., Goparaju, C., Franzoso, G., Lotze, M. T., Krausz, T., Pass, H.I., Bianchi, M.E., Carbone, M., 2010. Programmed necrosis induced by asbestos in human mesothelial cells causes high-mobility group box 1 protein release and resultant inflammation. *Proc. Natl. Acad. Sci. U. S. A.* 107, 12611–12616. doi:<http://dx.doi.org/10.1073/pnas.1006542107>.
- Zabler, S., Cloetens, P., Guigay, J.P., Baruchel, J., Schlenker, M., 2005. Optimization of phase contrast imaging using hard x rays. *Rev. Sci. Instrum.* 76, 073705 doi:<http://dx.doi.org/10.1063/1.1960797>.